energies

MDPI

Article

Hierarchical Modeling of the Thermal Insulation Performance of Novel Plasters with Aerogel Inclusions

Eugene D. Skouras [1,2,*], Georgia Tsolou [3] and Alexandros N. Kalarakis [3]

[1] Institute of Chemical Engineering Sciences, Foundation for Research and Technology-Hellas, GR-26504 Patras, Greece
[2] Fluid Mechanics & Turbomachinery Laboratory, Department of Mechanical Engineering, School of Engineering, University of the Peloponnese, GR-26334 Patras, Greece
[3] Laboratory of Materials and Structures Analysis, Department of Mechanical Engineering, School of Engineering, University of the Peloponnese, GR-26334 Patras, Greece; gtsolou@uop.gr (G.T.); alexandros.kalarakis@uop.gr (A.N.K.)
* Correspondence: eskouras@uop.gr or eugene.skouras@iceht.forth.gr

Abstract: Silica aerogel possesses a significantly lower thermal conductivity compared to still air at room temperature, thanks to its high porosity and advanced thermal and physical properties. It is extensively investigated for its potential use as an insulation material, usually being incorporated into other matrix materials, such as cement plasters, to enhance the overall thermal performance with minimal weight load. The development of lightweight thermal insulation materials is a key step in reducing energy consumption in hot and cold environments during construction and in thermal equipment. The superior insulation capabilities of aerogels stem from their nanostructured SiO_2 framework, which induces nanoscale rarefaction effects on the enclosed air near the SiO_2 structure. This study reconstructed the nanostructured SiO_2 network of modern aerogels using microscopy imaging and the literature data and integrated it into sophisticated heat transfer simulations at a microscopic level to predict its thermal performance. The simulation assumed conduction as the primary energy dissipation mechanism, incorporating local rarefaction effects based on kinetic theory approaches. SiO_2 aggregates were modeled as interconnected strings of spherical beads, with variations in the aggregate size explored in a parametric study. Nanoscale rarefaction phenomena, such as slip wall and Knudsen diffusion, prevalent at these grain sizes and structures, were incorporated to refine the modeling approach. The degree of the aerogel content relative to the effective properties of the multiphasic material was then investigated systematically along the multilayered mortar thickness and on a representative multiphasic layer at the mesoscopic level. The results quantify the significant decrease in the thermal conductivity of the heterogeneous material as the porosity of the aerogel increased. The insulation performance of this aerogel incorporated into cement plasters was assessed with this hierarchical approach and validated against experimental data, providing insights for the optimization of the fabrication process and potential applications in construction.

Keywords: silica aerogels; thermal insulation; heat-transfer modeling; microstructure reconstruction

Citation: Skouras, E.D.; Tsolou, G.; Kalarakis, A.N. Hierarchical Modeling of the Thermal Insulation Performance of Novel Plasters with Aerogel Inclusions. *Energies* **2024**, *17*, 5898. https://doi.org/10.3390/en17235898

Academic Editor: Carlos Miguel Costa

Received: 8 October 2024
Revised: 14 November 2024
Accepted: 15 November 2024
Published: 24 November 2024

1. Introduction

Silica aerogel, a contemporary lightweight material, boasts exceptional thermal insulation properties [1]. It is typically produced through sol–gel chemical processing and supercritical drying technologies. Initially, silicon dioxide is converted into a gel with the aid of water, followed by a drying process, where it is heated in a reactor at elevated temperatures of about 250 °C, exerting a pressure much greater than the atmospheric one.

Thus, air replaces the liquid components, and a cellular structure is formed, with a supporting SiO_2 framework structure with nanoscale dimensions, depending on the fabrication process. The combination of the nanophasic SiO_2 framework surrounded by air provides a thermal conductivity significantly lower than that of stagnant air at room temperature, while its porosity can reach up to 99%. The enhanced thermal insulation performance is attributed to the nanostructured network of SiO_2 particles, which facilitates nanoscale rarefaction phenomena as the primary heat transfer mechanisms for the enclosed air near the SiO_2 framework [1,2]. Consequently, there is considerable interest in its utilization as an insulator in construction technologies, due to these advanced thermal and physical attributes [3–5].

There are other types of aerogels with similar properties already available on the market, such as resin or cellulose aerogels [6,7], graphene aerogels [8], and carbon aerogels [9]. Cellulose aerogel is produced through the detachment of cell fibers using compressing paper and mixing it with water. A polymer resin is added, and a solution is made using a sonication process. Finally, the solution is placed in molds to dry and baked until it reaches about 120 °C [10]. Graphene and carbon aerogels are produced in a similar fashion. However, silica aerogel is considered more efficient for thermal insulation processes [5,11], and this aerogel structure is studied here.

In this study, the nanostructured SiO_2 network of modern aerogels was reconstructed, using microscopy imaging and data from the literature, and incorporated into sophisticated heat transfer simulations to predict their thermal behavior. The thermal conductivity of the novel material was determined using the heat flow method, and a theoretical model was developed to comprehend its behavior and predict its thermal properties [12]. The authors developed a simulator capable of predicting the thermal behavior, specifically the equivalent coefficient of thermal conductivity, of a commercially available aerogel product. This simulator considered the structure and composition of the produced aerogel, which was based on the relevant characterization data obtained by colleagues.

The simulation assumed conduction heat transfer as the predominant energy dissipation mechanism, incorporating local rarefaction phenomena from kinetic theory approaches while neglecting radiative heat transfer, although this could be included if necessary. Mesoscopic SiO_2 aggregates were modeled as intertwined strings of spherical beads with or without overlapping monomers, with the agglomerate size being investigated in a parametric study. Nanoscale rarefaction phenomena, such as slip wall and Knudsen diffusion, were implemented in the modeling because of their effects at these grain sizes and structures, breaking down the conventional continuum approach to convection.

The insulation performance of this aerogel structure incorporated into cement plasters was investigated and validated through comparison with experimental data, and recommendations are provided for tailoring the fabrication processes and potential usage in construction and thermal equipment.

The SiO_2 nanoparticles, or mesoscopic particles, are arranged in ordered rows of clusters or aggregates, as depicted in Figure 1 [1,13,14]. These mesoscopic aggregates are represented in simulations as spherical beads (depicted in green). The sizes of these aggregates, as indicated by the green particles, range from approximately 0.1 to 1 μm. The characterization and analysis of these beads focuses on the number of monomers arranged in a row, with a coordination number of up to two between intersections, where the coordination number exceeds two. The level of overlap between successive monomers was systematically examined to understand its impact on the effective heat transfer coefficient (k_{eff}).

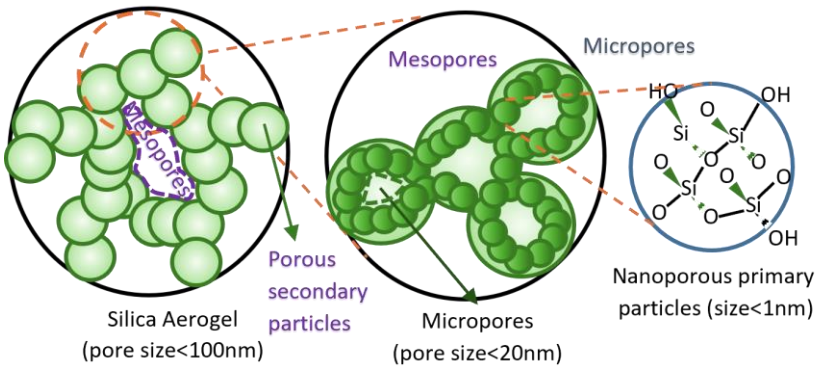

Figure 1. Microstructure of silica aerogel. (Left) Mesopores observed in the interstitial space of a framework composed of porous secondary particles. (Middle) Micropores found among a network of primary particles within each secondary particle. (Right) Nanoporous primary SiO_2 particles.

2. Materials and Methods

2.1. Microscale Reconstruction and Simulation of Silica Aerogel with CFD Methods

During modeling, conduction heat transfer is assumed as the primary mechanism for energy propagation. While convection is currently considered negligible, it can be incorporated into the modeling if that is required by the conditions [15–17]. The aggregates are represented as spheres made of SiO_2, with air serving as the bulk fluid [12,18,19]. The thermal conductivity ratio between the spheres and air is approximately 53 (at an average temperature of 25 °C). The diameter of the monomers is denoted as R_0, which is 10 nm. A temperature difference, denoted as ΔT, of 1 °C is applied along the main direction (x), while periodicity or symmetry conditions are prescribed along the transverse directions (y,z).

2.1.1. Description of Microscale Conditions of Silica Aerogel

The commercially available silica aerogel for plasters (type Cabot) exhibits a heat transfer coefficient of approximately k_{Cabot} ~19 mW/m K [20,21]. In comparison, the heat transfer coefficient of air is approximately k_{air} ~25 mW/m K, which is greater than k_{Cabot}. Consequently, the thermal conductivity of SiO_2, k_{SiO2}, is estimated ca. 50 mW/m K, with k_{air} being significantly greater than k_{Cabot}. This disparity is attributed to the high dilution effects at the nanoscale observed in the grain sizes of the aerogels [22].

Microscale simulations must consider these nanoscale effects, including rarefaction, thinning, and wall slip (Knudsen layers), which are mechanisms of gas theory that do not entirely conform to continuum equations [22,23]. The impact of rarefied conditions on the local heat transfer coefficient of a gas near a wall surface is quantified through parameters such as the local Knudsen number (Kn), the Prandtl number (Pr), the thermal accommodation coefficient of the wall (a), and the ratio of specific heats of the gas under constant pressure and volume, γ [22–25].

$$k_g = \frac{k_g^0(T)}{1 + 2\frac{2-a}{a}\left(\frac{2\gamma}{\gamma+1}\right)\frac{1}{Pr}Kn}, \quad (1)$$

or

$$k_g = \frac{k_g^0(T)}{1 + 2\zeta Kn}, \quad (2)$$

ζ~2 in air [16,22]. The Knudsen number (Kn) is defined as the ratio of the mean free path between successive collisions of gas molecules and a characteristic or average distance between walls, as follows:

$$Kn = \frac{\lambda}{D_{air}}. \quad (3)$$

The diameter, D_{air}, of an equivalent spherical pore with the same volume is assumed as a characteristic wall-to-wall distance. Gas theory can be used to express the mean free path between collisions as follows [26]:

$$\lambda = \frac{1}{\sqrt{2}\pi D_g^2 n_g} = \frac{k_B T}{\sqrt{2}\pi D_g^2 P}, \quad (4)$$

with k_B as the Boltzmann constant, D_g as the collisional cross-section diameter of the gas molecule, and T, P, and n_g as the local temperature, pressure, and number density, respectively. Kn < 0.01 indicates the continuum regime, usually addressed with Navier–Stokes descriptions with typical no-slip solid boundary conditions, while Kn in the (0.01, 0.1) range characterizes the slip flow regime, i.e., Navier–Stokes with slip description on solid walls [27]. Kn in the (0.1, 10) range indicates the transition regime, and Kn > 10 denotes the free molecular flow or diffusion counterpart. These limits indicate the order of magnitude, rather than precise values, of the Kn range of each regime, which vary with the application. Calculations with the proposed reconstructions have shown Kn to be in the 0.1–0.5 range, the upper values of the slip flow regime, and the onset of the transition range. Thus, continuum approaches have been used modified to accommodate slip and rarefaction phenomena [24,25,28].

2.1.2. Microscale Data, Design, and Simulation Parameters

The specific star-type design allows the number of spheres (monomers) in a unit cell to be a linear function of the number of successive particles in a chain between junctions/nodes, n_{chain},

$$N_{sph} = \alpha_{coord} n_{chain} - \beta_{period}, \quad (5)$$

with n_{chain} typically larger than 2 for such a fragment to be considered a chain. α_{coord} has the value 8, the number of connections along the diagonal cubic directions, i.e., the coordination number of the central (cross-link) monomer, and β_{period} = 2 × 3 = 6 accounts for the periodic conditions at the three principal directions (axes). The volume of each monomer of radius R_0 is assumed to have a spherical form,

$$V_{sph} = {}^4/_3\,\pi R_0^3. \quad (6)$$

The size distribution of the monomers is assumed to be uniform, and thus, all spherical monomers have the same radius, R_0. Overlapping between successive monomers is taking place, provided the distance between successive sphere centers, $dr_{i,i+1} = |r_i - r_{i+1}|$, is prescribed to be less than $2R_0$. For simplicity, and without any loss of generality, $dr_{i,i+1}$ is also assumed to be uniformly distributed. The total number of overlapping sections between successive monomers in a cell is trivially calculated as follows:

$$N_{over} = \alpha_{coord} n_{chain} + 2\beta_{period}, \quad (7)$$

and the volume of each overlap is

$$V_{over} = {}^4/_3\,\pi dr^2(3 - dr)R_0^3. \quad (8)$$

The star-shape form of the configuration of the particulates and a low value of the overlapping distance, dr, ensures that the coordination number of each particulate monomer is also the number of overlapping sections of each spherical body; that is, there are no three-body overlaps. The volume of air in a unit cell is

$$V_{air} = {}^1/_3\left[L_0^3 - \left(n_{sph}V_{sph} - n_{over}V_{over}\right)\right]. \quad (9)$$

The individual spherical-type pockets of air in the proposed unit cell are equal to the number of principal axes of the system, i.e., 3, and that is the value of the denominator in Equation (9). The hydraulic diameter of the air volume in a unit cell, i.e., the diameter of a spherical pore with equal volume, is

$$D_{air} = 2\sqrt[3]{3V_{air}/4\pi}. \quad (10)$$

The volume fraction of air in a unit cell, vf_{air}, is

$$vf_{air} = 3V_{air}/L_0^3. \quad (11)$$

The collisional cross section of air molecules at STP is $D_g = 3.789 \times 10^{-10}$ [m], and the porosity is ~85–90%. The effective conductivity is calculated from the temperature field of the solution through

$$k_{eff} = (Q_x/A_x)/(\Delta T_x/L_x), \quad (12)$$

$$Q_x = \overline{\int_{A_x} q_x dA}. \quad (13)$$

ΔT_x, A_x, and L_x represent the prescribed temperature difference between the inlet and outlet faces, the cross section, and the unit cell length across the heat flow direction (x), respectively. q_x is the total local heat flux calculated at any cross-sectional face dA. Q_x is averaged over the inlet and outlet faces.

The temperature boundary conditions ΔT_x applied on the microstructures reflect the periodic nature of the microscopic reconstructions. They are not designed to reflect the environment of actual thermal processes. They are used to extract the effective conductivity values, as given in the typical definition, Equation (12), in a typical environment.

2.2. Mesoscale Prediction of Thermal Properties of Cement Mortars with Aerogel Inclusions

The mesoscale simulations of the thermal behavior of various cement mortar compositions have been performed as follows. The conductivity of the aerogel was extracted from the microscale simulations. The conductivity of the cement paste that potentially included other additives, such as perlites, was obtained from the pertinent literature sources, along with the estimation of the effective thermal conductivity of the final product using scanning electron microscopy (SEM) data [13]. These data have been used as input to thermal characterization studies (conductivity estimations) of a cement mortar with the specific aerogel inclusions. Computations included the numerical solution of the conduction–convection equation directly through CFD [16], and the utilization of analytical expressions through Effective Medium Theory (EMT) approximations [15,29]. The analytical phase homogenization approaches for the effective conductivity, k_{eff}, of the same composite medium using Effective Medium Theory included Mori–Tanaka type models [30], as follows:

$$k_{eff} = k_{paste} + \frac{3\phi_{agg}k_{paste}(k_{agg} - k_{paste})}{3k_{paste} + \phi_{paste}(k_{agg} - k_{paste})}, \quad (14)$$

where ϕ_i and k_i are the volume fractions and thermal conductivities of phase i, respectively, with i as the aggregate (*agg*) or the paste (*paste*) phase, accordingly.

In view of the increased complexity of the mesoscale representations of multiphasic materials, and for reasons of minimal computational cost and increased accuracy of the resulting CFD simulations, the mesoscale investigations were divided into two representative configurations. One configuration pertained to the study of the thermal behavior of the multilayered material along its macroscopic heat gradient (paste thickness or depth), with the inclusions equidistantly distributed within. This was studied on a 2D

principal plane that included the direction along the thickness (depth), z, and one direction transversal to the heat gradient (for instance, x), with the assumption that its other transversal direction (y) was infinite, that is, translationally periodic, Figure 2. The second route was the 3D reconstruction of a representative layer of the material with randomly distributed spherical aerogel inclusions within and its study using 3D heat flow calculations, assuming translational periodicity on the outer boundaries, Figure 3.

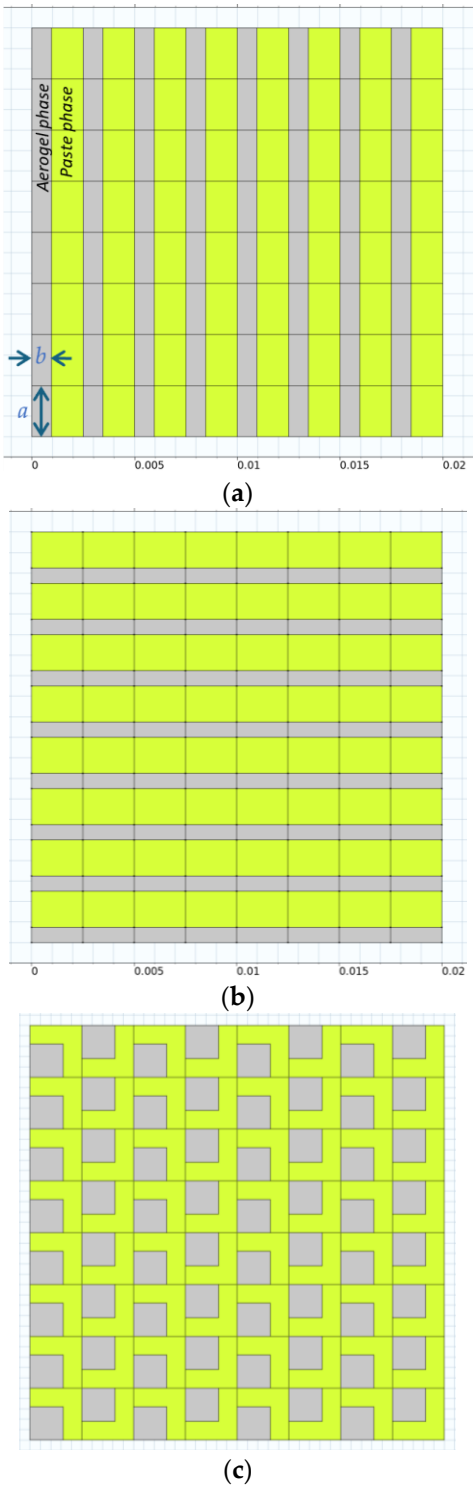

Figure 2. Three-dimensional CFD simulation domain configurations, (**a**) resistances in series, (**b**) resistances in parallel, (**c**) and dispersed (encapsulated) phase in continuous (encapsulating) phase.

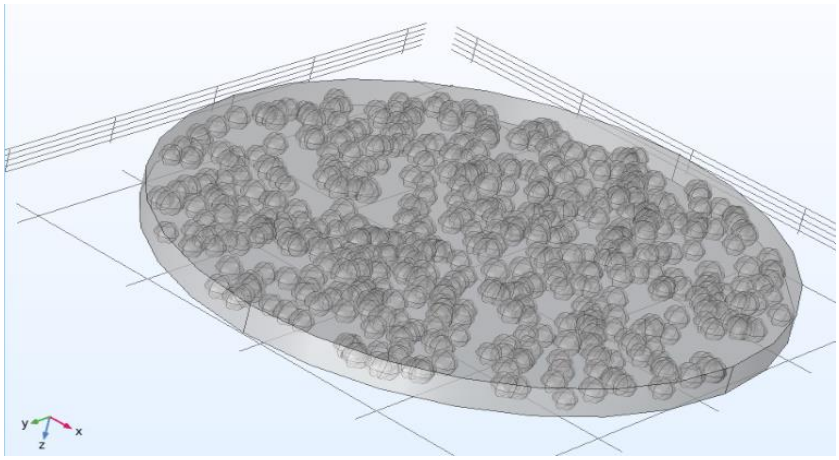

(**a**)

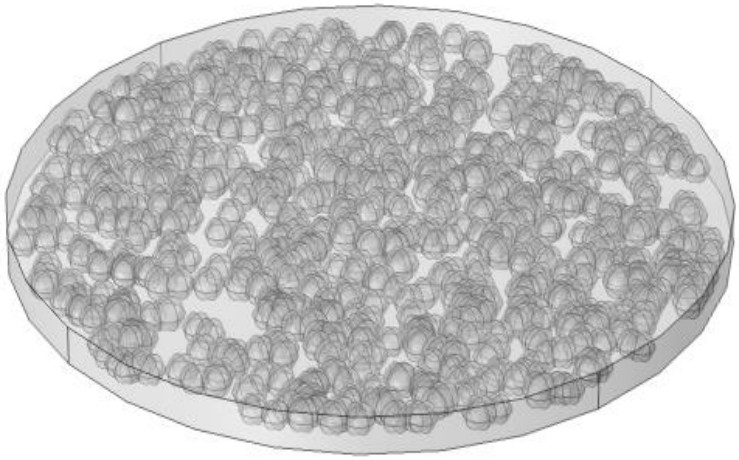

(**b**)

Figure 3. Three-dimensional representation of new aerogel product mortar (pellets) in paste (matrix). Monolayer material, aerogel volume fraction: (**a**) 30.3%, (**b**) 41.1%.

The boundary conditions applied on the mesoscopic simulations also were not intended to reflect actual simulation environments. They were used to extract the overall effective conductivity value, and allow comparing it with the experimental values in an effective formulation, i.e., measured in typical conditions following a typical measuring protocol. They were supposed to reflect the BCs of the microscopic simulations, since this is a prescription of the hierarchical approach used, i.e., using typical and similar BCs across scales.

2.2.1. Two-Dimensional Mesoscale Calculations of Effective Properties Along the Depth

The heat flux, Q_x, of the multilayered material was calculated from the finite element CFD simulations on reconstructed specimens, with the two material phases fully defined spatially [15,31], as in Figure 2a–c. This was entered into Equation (12), where the k_{eff} of the composite was calculated as if it was a homogeneous phase having the same thermal behavior.

The geometry of the final composition of the cement mortar was simulated on the computer either as a composition of phases in series, Figure 2a, a composition of phases in parallel, Figure 2b, or as one of the phases enclosed in the other one, which acts as a binder, Figure 2c.

The design and operating parameters for the 2D simulations are given in Table 1. The variation in the values of parameters specific to the design of parallel and series resistance

connections and of the dispersed (encapsulated) aerogel phase in continuous (encapsulating) paste phase formulations is also noted therein.

Table 1. Parameters for 2D CFD simulations.

Parameter	Value/Formula	Description
L	20 mm	total length of representative specimen
n	8	number of monomers per direction
a	L/n	unit cell length
ϕ	0–100%	volume fraction of the aerogel phase
k_{aero}	0.019 W/m K	thermal conductivity of aerogel
$k_{plaster}$	0.45 W/m K	thermal conductivity of paste
$T_{upstream}$	300 K	temperature at upstream face (along the imposed temperature gradient)
$T_{downsteam}$	$T_{upstream}$-1 K	temperature at downstream face (along the imposed temperature gradient)
Thickness of the aerogel phase according to the design configuration:		
b	$a\,\phi$	resistances in series or parallel
b	$a\sqrt{\phi}$	dispersed phase in continuous phase

The first case, connecting phases in series, acting as resistors in series, was excluded since it provided effective conductivities at the limit of the lowest conductivity, that of the aerogel, which were deemed unnaturally low, since the conductivities of such products are higher than the smallest value of its components. An alternative plan was also considered, phases in parallel, in the form of resistors in parallel. This configuration was also found to provide very high values, close to the highest value of its components (paste), since the conductivities of such products are smaller than this value.

Series and parallel interconnection scenarios were found to give the lower and upper bounds on the effective conductivity of the final product. The plan with an enclosed phase and interconnected thermal transport paths from the enclosed phase was found to provide effective conductivity results close to the measured values.

2.2.2. Three-Dimensional Mesoscale Calculations of Effective Properties in a Representative Layer

Three-dimensional digital samples of a layer of cement mortar were fabricated with the aerogel particles assumed to be spherical inclusions containing SiO_2 frameworks with air pockets, randomly immersed in a paste matrix [14], as shown in Figure 3. Sphere overlapping was allowed during deposition of the aerogel inclusions, and the volume fraction of the aerogel was estimated taking into account two- and three-particle overlaps. The main solid volume was the cement mortar, which has been designed as a cylindrical slab of periodic conditions. Cylindrical geometry was chosen in order to avoid the corner effects of symmetry boundary conditions on primary axes. The thermal conductivities were set at (k_{aero}, k_{paste}) = (0.005, 0.470) [W/m K], in accordance with the lower values of the commercial aerogel properties obtained through the microscale simulations, as discussed in the previous sections.

The volume of the cylindrical domain used in the present simulations was fixed, V_{cyl} = 0.0034975 μm^3. The total volume and number of spherical inclusions depend on the porosity of each realization. The temperature difference between the external faces along the vertical y axis was set at a fixed value (ΔT = 1 °C), whereas the material properties along the horizontal x and z axes were implemented as periodic through pertinent Newmann-type zero-flux boundary conditions.

3. Results

3.1. Microscale Reconstruction and Analysis of Aerogel

The domain was meshed with unstructured elements in the present simulations, as follows: The minimum and maximum mesh elements were set at $R_0/20$ and R_0, respectively. In order to accommodate the elevated temperature gradients at the solid–air interfaces, the number of boundary layers at faces normal to the heat flow direction was set at three. This resolution displayed mesh-independent result behavior. Mesh independence is shown at later simulation stages of the final structures proposed by this work.

Figures 4–7 depict the reconstructions and corresponding performances of silica aerogels using the aforementioned method with gradually increased complexity. Monomers were assumed to have the k_{SiO2} thermal conductivity value, whereas the air was attributed with the respective k_g value, Equation (2), after extraction of the pertinent Kn through Equation (3), with its terms λ and D_{air} calculated by Equations (4) and (10), respectively.

Figure 4a portrays an aerogel structure with four monomers existing between junctions (on a chain), referred to as StructureType#1, shown as spherical particles overlapping with $dr = |r_i - r_{i+1}| = R_0/10$, thus $ol = 0.1$. The coordination number of junction (crosslink) elements, a_{coord}, was six. The reconstructed cell was symmetric and periodic. The temperature distribution found with the rarefied CFD simulations was typical for such processes.

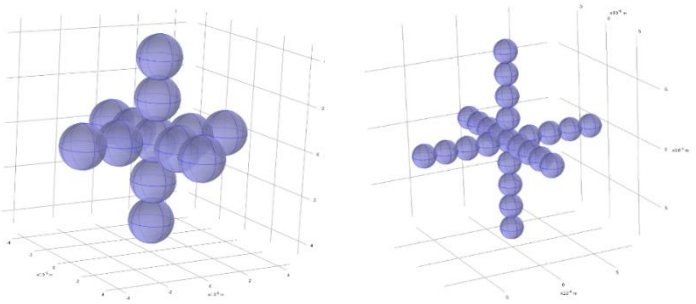

(**a**) (**b**)

Figure 4. (**a**) StructureType#1: $n_{chain} = 4$, $a_{coord} = 6$, $ol = 0.1$. (**b**) StructureType#2: $n_{chain} = 8$, $a_{coord} = 6$, $ol = 0.1$.

Figure 5 presents the thermal performance predictions of the StructureType#1 reconstruction simulations with gradually increasing overlapping levels (ol). k_{eff} intensifies as the ol increases, since there are gradually more connected faces of the solid medium for the heat flow path to pass through, bypassing the thermal resistance of the air. However, the volume fraction of air is extremely high, compared to the Cabot aerogel regime of 85–90%, at most overlapping cases, except for the most extreme one ($ol = 0.75$). Moreover, it is evident that this structure configuration cannot achieve the value of the Cabot aerogel $k_{eff} = 0.019$ W/m K, even in the most extreme overlapping case, that of $ol = 0.75$. The latter ol case is considered extreme, since there are now three-body overlapping sections present at the junction monomers, which is not usually addressed physically because of the framework-type configuration of the SiO_2 aerogel form. It is also unrealistic considering the SEM images of these types of aerogels that clearly do not display this level of overlapping between granules [2,13].

In order to overcome these limitations, structures of alternative configurations were reconstructed, with properties tailored to the thermal conditions at hand. Figure 4b presents an aerogel structure, StructureType#2, with more chain monomers between junctions than StructureType#1. Eight (8) chain particles between intersections were implemented for StructureType#2, and the coordination number of junction elements was six (6). As shown in Figure 4, the overlapping spheres were set at $dr = R_0/10$ ($ol = 0.1$). The unit

cell of StructureType#2 was symmetric and periodic. Table 2 presents the insulation performance of the characteristic StructureType#2 structures, which were still lower than the aerogels. It is evident that these structures suffered from the unphysical existence of a dominant heat flow path with connected spheres along the main heat flow direction, which still make the effects of the rarefied air phenomena relatively insignificant.

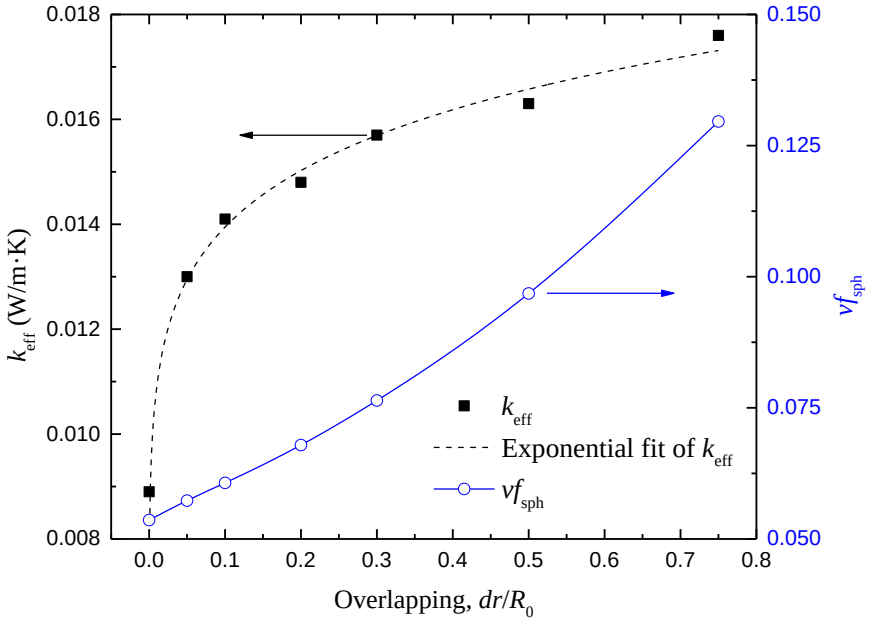

Figure 5. Simulation results for StructureType#1 for gradually increasing overlapping *ol* (*dr*/*R*0).

Table 2. Simulation results for StructureType#2 (Figure 4).

ol **[-]**	k_{eff} **[W/m K]**	vf_{sph} **[-]**
0.0	0.011	0.018
0.1	0.013	0.020

Figure 6a presents an aerogel structure with non-overlapping elements (*dr* = 0) and two (2) chain monomers. The coordination number of junctions is four (4), and the unit cell is symmetric and periodic. This is a densely packed structure, with increased difficulty due to the single-point contacts between successive spheres; however, it is within the simulation limits of the method.

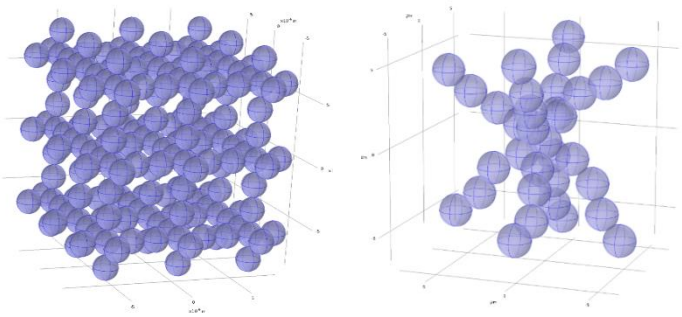

(**a**) (**b**)

Figure 6. (**a**) StructureType#3: n_{chain} = 2, a_{coord} = 4, *ol* = 0, symmetric and periodic unit cell. (**b**) StructureType#4: n_{chain} = 8, a_{coord} = 8, *ol* = 0.1, randomized placement, asymmetric, and non-periodic unit cell.

In pursuit of a more physical distribution of silica monomers, structures without the existence of an unphysical dominant longitudinal path of silica monomers were built. Such a structure is shown in Figure 6b, having overlapping elements with $dr = R_0/10$ and eight (8) monomers between junctions. The coordination number of junctions was eight (8), with randomized placement of the monomers relative to each other, with an asymmetric and non-periodic unit cell. This was a randomly packed structure, with increased difficulty due to the multiple-point contacts and the volume exclusions at the junctional sphere; however, it was within the simulation limits of the method. The present structure had a $D_{air} = 7.45\ R_0$.

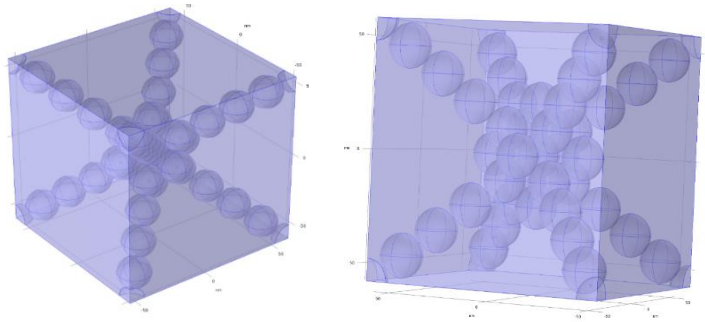

(**a**) (**b**)

Figure 7. StructureType#5: $n_{chain} = 9$, $ol = 1/200$, symmetric and periodic unit cell. $a_{coord} = 8$ (**a**), 14 (**b**).

The structure shown in Figure 7 has nine chain monomers and a symmetric and periodic unit cell, shown here with overlapping elements of $dr = R_0/200$. The coordination number at the junction is eight (8) in the left figure and fourteen (14) in the right one. A monomer is shared between unit cells. These structures pose increased difficulty due to the limiting overlapping, which necessitates refined resolution, as well as at the multiple-point contacts and the volume exclusions at the junctional sphere. However, these constrictions are within the simulation limits of the method. These reconstructions have the largest unobstructed free-volumes amongst the ones studied in this work (Figures 4–7), with a $D_{air} = 9.7R_0$, and were used for the final calculation and investigation.

Three-Dimensional Microscale Effective Properties of Aerogel

In the following results, simulations were performed of StructureType#5 reconstructions with the following setup. *dr*, the overlapping level of successive particles, was set as a fraction (*ol*) of R_0, R_0 at 10 nm, and the coordination number at the junctions was eight (8).

Convergence and mesh independence were checked using simulations with successively denser unstructured mesh, as follows: Minimum and maximum mesh element (nm): Resolution Level #1: 0.461/6.33, Resolution Level #2: 0.173/4.03, Resolution Level #3: 0.023/2.3. The boundary layers at faces normal to the heat flow direction were set at three (3). The implemented boundary-layer stretching factor was 1.25.

The simulations converged and were mesh independent for all practical purposes using either finer, extra fine, or extremely fine resolutions, as shown in Table 3. The $n_{chain} = 5$ and $ol = 0.005$ part of StructureType#5 was shown to be the most promising structure attaining the heat transfer coefficient of the Cabot aerogel reported at the upper porosity regime, 0.89 [21], while the $n_{chain} = 4$ and $ol = 0.005$ (or 0.010) could achieve this at a lower porosity level, 0.83.

Table 3. Simulation results for StructureType#5.

	k_{eff}/k_m	k_{eff} [W/m K]	vf_{sph}
n_{chain} = 4			
ol = 0, Resolution Level #3	0.620	0.0159	0.170
ol = 0, Resolution Level #2	0.628	0.0159	0.170
ol = 0, Resolution Level #1	0.625	0.0160	0.170
ol = 0.005, Resolution Level #1	0.934	0.0239	0.171
ol = 0.010, Resolution Level #1	1.094	0.0280	0.173
n_{chain} = 5			
ol = 0, Resolution Level #1	0.551	0.0141	0.109
ol = 0.005, Resolution Level #1	0.735	0.0188	0.110

Resolution Level #1: min/max elem. size = 0.461/6.33 nm. Resolution Level #2: min/max elem. size = 0.173/4.03 nm. Resolution Level #3: min/max elem. size = 0.023/2.3 nm.

3.2. Mesoscale Results of Multphasic Cement Mortal with Aerogel Inclusions

3.2.1. Two-Dimensional Mesoscale Effective Properties Across the Depth

Cement mortars with silica aerogel inclusions that were fabricated and characterized by colleagues through collaboration (private communications) were reconstructed and subsequently simulated with the mesoscale methodologies proposed in the present work. The simulation results, along with sample characterization results, as well as an equivalent medium approach, are presented in Figure 8. For the physicochemical data values, such as apparent densities and component ratios, sample-specific characterization data obtained from collaborating partners were used.

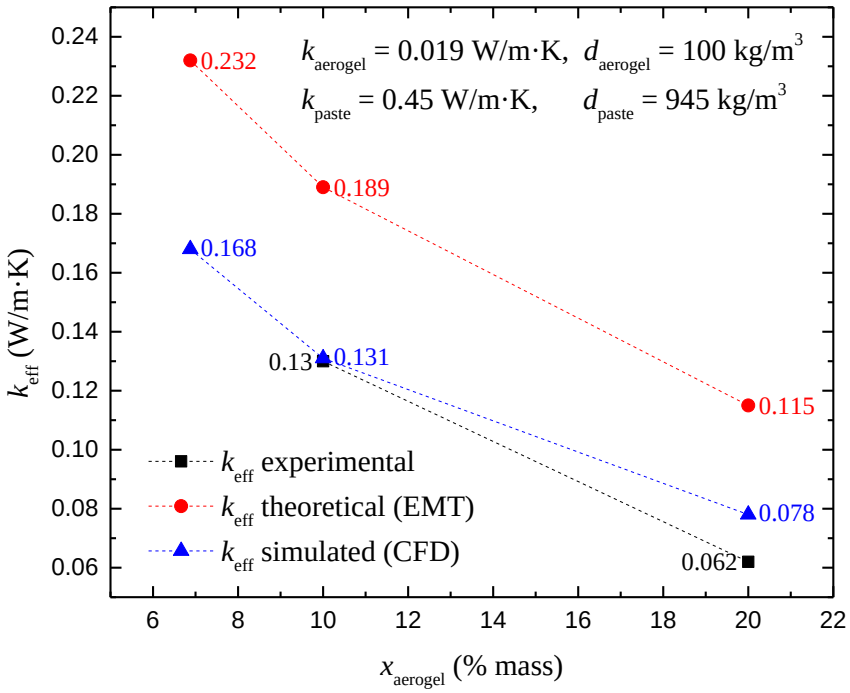

Figure 8. Mesoscale CFD results and analytical expressions (EMT) in comparison with characterization results (private communication with partners).

The comparison with the characterization results can be considered satisfactory, while the theoretical estimates also provide accurate results, although less close to the experimental ones, especially at an elevated aerogel content. Improved approximations could be made using more specific and optimal paste and aerogel physicochemical data;

however, this was not pursued in the present work, since these were not available for the present material.

3.2.2. Three-Dimensional Mesoscale Effective Properties of a Representative Layer

The isotherms of temperature distribution in a thin section of the new mortar are shown in Figure 9. Table 4 provides the effective conductivity estimations through the 3D simulations. The convergence and mesh-independence analysis is also shown therein.

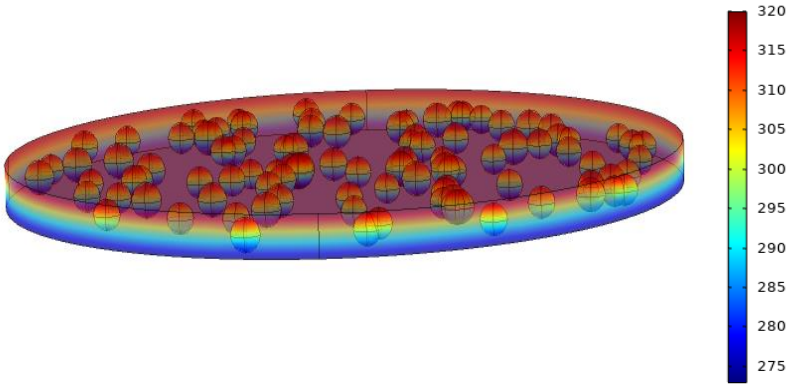

(**a**)

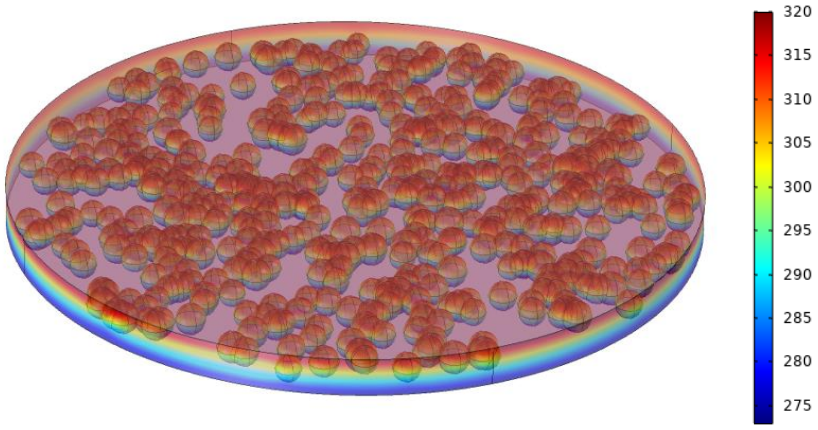

(**b**)

Figure 9. Isotherms of temperature distribution in the new mortar. Monolayer material, aerogel volume fraction: (**a**) 7.3%, (**b**) 30.3%.

Table 4. Equivalent conductivity with aerogel content (volume fraction).

#Aerogel Spheres	Resolution Level	V_{cyl}	$V_{aerogel}$	$vf_{aerogel}$	$x_{aerogel}$	k_{eff}
[-]		[μm³]	[μm³]	[% vol]	[% mass]	[W/m K]
10	#3	0.10053	0.0000078744	0.0078%	0.00083%	0.46996
100	#3	0.0034962	0.0002555	7.30%	0.826%	0.43609
500	#3	0.0034962	0.0010598	30.3%	4.398%	0.32842
800	#3	0.0034962	0.0014371	41.1%	6.877%	0.27813
800	#2	-"-	-"-	-"-	-"-	0.26368
800	#1	-"-	-"-	-"-	-"-	0.25159

Resolution Level #3: min/max elem. size = 0.003/0.325 nm. Resolution Level #2: min/max elem. size = 0.024/0.569 nm. Resolution Level #1: min/max elem. size = 0.065/0.894 nm.

The effect of the aerogel content on the thermal properties of the multiphasic material is displayed in Table 4 in a quantifiable manner. Higher volume fractions, which would result in more severe overlapping, were not pursued in the present work because of the complexity of the final geometry with many-body (higher than two) overlaps, which prohibited the systematic production of an accurate mesh for the resulting conglomerated entities. The trend towards the aerogel volume fraction required to increase the effective thermal insulation properties of the mortar sufficiently is portrayed. The effective conductivity of the multiphasic material in the highest content was lowered by nearly half the value of the clean cement paste, i.e., that of zero aerogel content. Thus, the proposed method can provide guidelines for the tailoring of the manufacturing route of such novel high-insulation light materials with optimum thermal properties.

The comparison of the two mesoscale methods, the 2D simulations along the thickness and the 3D reconstructions of a layer, portray a notable difference in the results, as seen at vf_{aerogel} = 41.1% vol, or x_{aerogel} = 6.877% mass, shown as the first data point of the CFD curve in Figure 8 and the rows with #Aerogel Spheres = 800 of Table 4. Given the validation of the 2D results with the experimental data, the 3D simulations are seemingly overestimating the thermal properties of the mixture, probably due to the increased paths of higher conductivity of the matrix around the spherical aerogel particles. The spherical form of the aerogels might not be the most relevant one in the final mixture, and orthogonal representations, in the form of the 2D realizations of the first mesoscale route, might be more relevant. However, this overestimation is deemed not significant for the estimation of the trend of the thermal properties for the cement mortar.

4. Conclusions

A simulator for the rarefied conditions of nanoparticulate silica aerogels was developed, and their insulation properties were investigated. Sophisticated structures that evade the existence of an unphysical dominant longitudinal path of silica monomers were reconstructed and investigated. The porosity was controlled by the number of particles in a chain between junctions/nodes, combined with the overlapping level between consecutive particles. The reduced k of the Cabot aerogel for a given porosity can be achieved, depending on the configuration and overlapping level.

The aforementioned microscopic data were used as one-way coupled input to mesoscopic simulation methodologies developed to assess the thermal properties of thermally insulating cement mortar, which is produced by adding aerogel inclusions to standard cement mortar and used as a plaster for covering buildings.

The degree of the aerogel content relative to the effective properties of the multiphasic material was investigated quantifiably along the multilayered mortar thickness (2D Cartesian reconstructions) and on a representative multiphasic layer (3D cylindrical reconstructions). The comparison of the 2D simulation results across the cement paste thickness with the characterization results can be considered satisfactory, while theoretical estimates using Effective Medium Theory approaches also provide conceptually useful results, although less accurate in comparison to the experimental ones, particularly at an elevated aerogel content.

The thermal simulations of these complex materials offer insight into the inherent mechanisms of each required mechanical and physicochemical property, and reconsider the configuration of these materials to understand how to enhance and optimally combine the required properties. The results have shown that the thermal conductivity of the heterogeneous material decreases significantly as the porosity of the aerogel increases, depicted either as spherical-shaped 3D nanoinclusions in each mortar layer, or as rectangular-shaped 2D nanophases along the thickness of the paste. The trend on the aerogel volume fraction required to lower the effective thermal transport properties of the novel cement mortar to a satisfactory level was depicted, offering the manufacturing of novel light mortars with tailored thermal insulation properties.

Thus, aerogel can be considered as a good insulator for the future, especially in applications where lightweight material usage is essential, with a wide range of thermal properties depending on the percentage of porosity chosen in each case. In conclusion, it is shown that aerogels can cover a wide range of thermal requirements. The simulations were able to follow the experimental results of the multiphasic cement mortars investigated in the present work, both with 2D and 3D approaches.

Technical solutions can apply the proposed simulations to predict the efficiency and performance of aerogel–cement plasters for specific thermal insulation applications. However, they should also take into account the mechanical stability and homogenization properties, along with mass production and large-size preparation improvements, of the final aerogel–cement plaster products, issues that should also be addressed in a comparable fashion.

Author Contributions: Conceptualization, E.D.S. and A.N.K.; investigation, E.D.S. and A.N.K.; methodology, G.T., E.D.S., and A.N.K.; software, G.T. and E.D.S.; supervision, E.D.S.; validation, G.T. and E.D.S.; visualization, E.D.S.; writing—original draft, E.D.S.; writing—review and editing, E.D.S. and A.N.K. All authors have read and agreed to the published version of the manuscript.

Funding: This work was supported by the project "Advanced, high-performance thermoinsulating plaster", (Acronym: AeroPlas) co-financed by the European Regional Development Fund of the European Union and Greek national funds under the framework of Hellenic NSFA 2014-2020 Operational Programme "Competitiveness, Entrepreneurship and Innovation", Action "RESEARCH—CREATE—INNOVATE", T2EDK-03219.

Data Availability Statement: The original contributions presented in the study are included in the article; further inquiries can be directed to the corresponding author.

Acknowledgments: The fabrication and characterization of novel cement mortars with aerogel additions were conducted by the M. Stefanidou group at Aristotle University and the G. Syriopoulos group of ISOMAT SA, while the T. Ioannides and V. Drakopoulos group at FORTH/ICE-HT is acknowledged for SEM imaging provisions and aerogel physicochemical data. Ch. Tsagaratou is acknowledged for assisting in 3D simulations of the novel insulation materials.

Conflicts of Interest: The authors declare no conflicts of interest. The funders had no role in the design of the study; in the collection, analyses, or interpretation of data; in the writing of the manuscript; or in the decision to publish the results.

References

1. Li, C.; Chen, Z.; Dong, W.; Lin, L.; Zhu, X.; Liu, Q.; Zhang, Y.; Zhai, N.; Zhou, Z.; Wang, Y.; et al. A review of silicon-based aerogel thermal insulation materials: Performance optimization through composition and microstructure. *J. Non-Cryst. Solids* **2021**, *553*, 120517.
2. Liang, Y.; Ding, Y.; Liu, Y.; Yang, J.; Zhang, H. Modeling Microstructure Effect on Thermal Conductivity of Aerogel-Based Vacuum Insulation Panels. *Heat Transf. Eng.* **2020**, *41*, 882–895.
3. Muthuraj, R.; Jimenez-Saelices, C.; Grohens, Y.; Seantier, B. Chapter 15 Applications of Polysaccharide and Protein Based Aerogels in Thermal Insulation. In *Biobased Aerogels: Polysaccharide and Protein-based Materials*; The Royal Society of Chemistry: London, UK, 2018; pp. 261–294.
4. Wang, L.; Liu, P.; Jing, Q.; Liu, Y.; Wang, W.; Zhang, Y.; Li, Z. Strength properties and thermal conductivity of concrete with the addition of expanded perlite filled with aerogel. *Constr. Build. Mater.* **2018**, *188*, 747–757.
5. Adhikary, S.K.; Ashish, D.K.; Rudžionis, Ž. Aerogel based thermal insulating cementitious composites: A review. *Energy Build.* **2021**, *245*, 111058.
6. Sen, S.; Singh, A.; Bera, C.; Roy, S.; Kailasam, K. Recent developments in biomass derived cellulose aerogel materials for thermal insulation application: A review. *Cellulose* **2022**, *29*, 4805–4833.
7. Cheng, H.; Xue, H.; Hong, C.; Zhang, X. Preparation, mechanical, thermal and ablative properties of lightweight needled carbon fibre felt/phenolic resin aerogel composite with a bird's nest structure. *Compos. Sci. Technol.* **2017**, *140*, 63–72.
8. Lin, Y.; Ehlert, G.J.; Bukowsky, C.; Sodano, H.A. Superhydrophobic Functionalized Graphene Aerogels. *ACS Appl. Mater. Interfaces* **2011**, *3*, 2200–2203.
9. Lee, Y.J.; Jung, J.C.; Yi, J.; Baeck, S.-H.; Yoon, J.R.; Song, I.K. Preparation of carbon aerogel in ambient conditions for electrical double-layer capacitor. *Curr. Appl. Phys.* **2010**, *10*, 682–686.
10. Huang, J.; Wang, X.; Guo, W.; Niu, H.; Song, L.; Hu, Y. Eco-friendly thermally insulating cellulose aerogels with exceptional flame retardancy, mechanical property and thermal stability. *J. Taiwan Inst. Chem. Eng.* **2022**, *131*, 104159.

11. Jia, G.; Guo, J.; Li, Z. Controllable preparation of aerogel/expanded perlite composite and its application in thermal insulation mortar. *Constr. Build. Mater.* **2023,** *394*, 132257.
12. Skouras, E.D.; Karagiannakis, N.P.; Burganos, V.N. Thermal Conduction in Hybrid Nanofluids and Aggregates. *Nanomaterials* **2024**, *14*, 282.
13. Ma, H.; Zheng, X.; Luo, X.; Yi, Y.; Yang, F. Simulation and Analysis of Mechanical Properties of Silica Aerogels: From Rationalization to Prediction. *Materials* **2018**, *11*, 214.
14. He, F.; Wang, Y.; Zheng, W.; Wu, J.Y.; Huang, Y.H. Effective thermal conductivity model of aerogel thermal insulation composite. *Int. J. Therm. Sci.* **2022**, *179*, 107654.
15. Abidi, S.; Nait-Ali, B.; Joliff, Y.; Favotto, C. Impact of perlite, vermiculite and cement on the thermal conductivity of a plaster composite material: Experimental and numerical approaches. *Compos. Part B Eng.* **2015**, *68*, 392–400.
16. Zhang, H.; Tan, Y.; Wang, G.; Nan, Y.; Wang, L. Development of a Numerical Model to Calculate Heat Transfer in a Cement-Based Material Incorporated with Expanded Perlite Filled with Aerogel. *Int. J. Thermophys.* **2020**, *41*, 148.
17. Bourantas, G.C.; Skouras, E.D.; Loukopoulos, V.C.; Burganos, V.N. Heat transfer and natural convection of nanofluids in porous media. *Eur. J. Mech. B/Fluids* **2014**, *43*, 45–56.
18. Zeng, S.Q.; Hunt, A.; Greif, R. Geometric Structure and Thermal Conductivity of Porous Medium Silica Aerogel. *J. Heat Transf.* **1995**, *117*, 1055–1058.
19. Liu, Q.; Deng, S.; Wang, Z.; Xie, L.; Wang, G.; Chen, Z.; Wu, X.; Li, Z. Hierarchically theoretical calculation and 3D reconstruction simulation of effective thermal conductivity for MTMS-based silica aerogels. *J. Sol-Gel Sci. Technol.* **2024**, *111*, 324–335.
20. Buratti, C.; Moretti, E.; Belloni, E. Aerogel plasters for building energy efficiency. In *Nano and Biotech Based Materials for Energy Building Efficiency*; Springer International Publishing, Switzerland, 2016; pp. 17–40.
21. Thorne-Banda, H.; Miller, T. Aerogel by Cabot Corporation: Versatile Properties for Many Applications. In *Aerogels Handbook*; Aegerter, M.A., Leventis, N., Koebel, M.M., Eds.; Springer: New York, NY, USA, 2011; pp. 847–856.
22. Wei, G.; Liu, Y.; Du, X.; Zhang, X. Gaseous Conductivity Study on Silica Aerogel and Its Composite Insulation Materials. *J. Heat Transf.* **2012**, *134*, 041301.
23. Hoseini, A.; McCague, C.; Andisheh-Tadbir, M.; Bahrami, M. Aerogel blankets: From mathematical modeling to material characterization and experimental analysis. *Int. J. Heat Mass Transf.* **2016**, *93*, 1124–1131.
24. Kalarakis, A.N.; Michalis, V.K.; Skouras, E.D.; Burganos, V.N. Mesoscopic Simulation of Rarefied Flow in Narrow Channels and Porous Media. *Transp. Porous Media* **2012**, *94*, 385–398.
25. Michalis, V.K.; Kalarakis, A.N.; Skouras, E.D.; Burganos, V.N. Rarefaction effects on gas viscosity in the Knudsen transition regime. *Microfluid. Nanofluidics* **2010**, *9*, 847–853.
26. Zeng, S.Q.; Hunt, A.; Greif, R. Mean Free Path and Apparent Thermal Conductivity of a Gas in a Porous Medium. *J. Heat Transf.* **1995**, *117*, 758–761.
27. Beskok, A.; Karniadakis, G.E. A model for flows in channels, pipes, and ducts at micro and nano scales. *Microscale Thermophys. Eng.* **1999**, *3*, 43–77.
28. Beskok, A. Validation of a new velocity-slip model for separated gas microflows. *Numer. Heat Transf. Part B-Fundam.* **2001**, *40*, 451–471.
29. Landauer, R. The Electrical Resistance of Binary Metallic Mixtures. *J. Appl. Phys.* **1952**, *23*, 779–784.
30. Böhm, H.J.; Nogales, S. Mori–Tanaka models for the thermal conductivity of composites with interfacial resistance and particle size distributions. *Compos. Sci. Technol.* **2008**, *68*, 1181–1187.
31. Wang, M.; Pan, N. Predictions of effective physical properties of complex multiphase materials. *Mater. Sci. Eng. R Rep.* **2008**, *63*, 1–30.